Micro-Raman spectroscopy for a comprehensive understanding of the structural evolution of Basaltic-Andesite and Trachybasalt multiphase systems

Chemical Geology

Micro-Raman spectroscopy for a comprehensive understanding of the structural evolution of Basaltic-Andesite and Trachybasalt multiphase systems

--Manuscript Draft--

Manuscript Number:	CHEMGE15282R1
Article Type:	Research paper
Keywords:	Magma; Glass; Raman Spectroscopy; Boson Peak; Viscosity; Multiphase Systems
Corresponding Author:	Michele Cassetta University of Verona Department of Computer Science ITALY
First Author:	Michele Cassetta
Order of Authors:	Michele Cassetta
	Francesco Vetere
	Marco Zanatta
	Diego Perugini
	Matteo Alvaro
	Beatrice Giannetta
	Claudio Zaccone
	Nicola Daldosso
Abstract:	The liquid viscosity of multiphase systems is usually retrieved by the use of combined chemical analysis and empirical chemistry-based models. Here we present an alternative approach to study the glassy pools in highly crystallized basalt-andesite samples obtained from isothermal crystallization experiment at different shear rates. Polarized micro-Raman spectra were collected at room temperature on the glassy portions. Results of residual glass structures from the high frequency region of Raman spectra show an increasing polymerization degree. The fragility, derived from the evolution of the boson peak, decreases according to the experimental time evolution. Also, the presence of nanolites in residual glasses adds a further degree of complexity that needs to be considered in the frame of melts polymerization and rheological behavior of volcanic systems. On this concern, the MYEGA formalism approach allows to retrieve the residual melt viscosity of the partly crystallized samples, avoiding its direct measurement and reducing the errors induced when general viscosity models, based only chemical data, are used. We validated our prediction by determining the low-temperature viscosity data converting, through known shift factors, the thermograms obtained by differential scanning calorimetry. This study provides a further route in characterizing multiphase systems, also including the effect of nanosized crystals, and offers the possibility of increasing the spatial resolution through microscopy and ridding viscosity parametrizations of invasive and time-consuming operations.

Micro-Raman spectroscopy for a comprehensive understanding of the structural evolution of Basaltic-Andesite and Trachybasalt multiphase systems

Michele Cassetta[1,§], Francesco Vetere[2], Marco Zanatta[3], Diego Perugini[4], Matteo Alvaro[5], Beatrice Giannetta[6], Claudio Zaccone[6,7] and Nicola Daldosso[1]

[1]*Department of Computer Sciences, University of Verona, I-37134 Verona, Italy*

[2]*Department of Physical Sciences, Earth and Environment, University of Siena, I-53100, Siena, Italy*

[3]*Department Physics, University of Trento, I-38123 Trento, Italy*

[4]*Department of Physics and Geology, University of Perugia, I-06100 Perugia, Italy*

[5]*Department of Earth and Environmental Sciences, University of Pavia, I-27100, Pavia, Italy*

[6]*Department of Biotechnology, University of Verona, I-37134 Verona, Italy*

[7]*National Institute of Geophysics and Volcanology, I-00143 Roma, Italy*

[§]Author for correspondence:

Dr. Cassetta Michele,

E-Mail: **michele.cassetta@univr.it**

ABSTRACT

The liquid viscosity of multiphase systems is usually retrieved by the use of combined chemical analysis and empirical chemistry-based models. Here we present an alternative approach to study the glassy pools in highly crystallized basalt-andesite samples obtained from isothermal crystallization experiment at different shear rates. Polarized micro-Raman spectra were collected at room temperature on the glassy portions. Results of residual glass structures from the high frequency region of Raman spectra show an increasing polymerization degree. The fragility, derived from the evolution of the boson peak, decreases according to the experimental time evolution. Also, the presence of nanolites in residual glasses adds a further degree of complexity that needs to be considered in the frame of melts polymerization and rheological behavior of volcanic systems. On this concern, the MYEGA formalism approach allows to retrieve the residual melt viscosity of the partly crystallized samples, avoiding its direct measurement and reducing the errors induced when general viscosity models, based only chemical data, are used. We validated our prediction by determining the low-temperature viscosity data converting, through known shift factors, the thermograms obtained by differential scanning calorimetry. This study provides a further route in characterizing multiphase systems, also including the effect of nanosized crystals, and offers the possibility of increasing the spatial resolution through microscopy and ridding viscosity parametrizations of invasive and time-consuming operations.

Introduction

Magmas are multiphase systems mainly composed of melt, crystals, and exsolved volatiles (i.e. bubbles). The viscosity of magmas is central in determining their time scale deformation and the relaxation time of the melt as they near Earth surface (Dingwell, 1996; Gonnermann and Manga, 2007; Papale, 1999; Zhang, 1999). The parametrization of these mechanisms is a necessary addition to the current conceptualization of volcanic hazard (Newhall and Punongbayan, 1996; Taddeucci et al., 2021). In particular, the interplay between the melt and the solid fraction (Φ) controls the apparent viscosity (η_{app}). Indeed, crystallization and resorption phenomena modify the structure and chemistry of the melt leading to an increase of η_{app}. Variations of pressure (P), temperature (T), chemistry (χ) and oxygen fugacity ($f\,O_2$) might produce non-linear effects on the rheological evolution of magmas and melts influencing nucleation and crystal growth rates as well as resorption.

Such a complex scenario represents a considerable challenge in modeling the rheology of crystal-bearing multi-phase systems (Caricchi et al., 2007; Liu et al., 2018; Mader et al., 2013; Vona et al., 2011). Several limits rise when the shear rate and the undercooling are considered as driver parameters in predicting the rheology of magmas (Kolzenburg et al., 2020; Vetere et al., 2022, 2019). Conversely, the efforts in parametrizing the T-dependence of the pure liquid viscosity (η_l) have provided more accurate models (Giordano et al., 2008; Hui and Zhang, 2007; Mauro et al., 2009; Shaw, 1972) that are crucial in predicting flow properties as a function of the relative viscosity (η_r), which is the ratio $\eta_r = \eta_{app}/\eta_l$. A fundamental process to take into account is the evolution of Φ that directly affects chemistry and structure of the residual melt (i.e. polymerization), causing a change in the viscosity of the carrying phase, even by orders of magnitude (Di Genova et al., 2020; Dingwell et al., 1998; Whittington et al., 2001). This information can be retrieved by investigating the vitrified part obtained after the fast quenching of the melt in eruptive products including either lavas or lapilli. This information can be obtained after the quenching of dynamics crystallization experiments as well (see (Vetere et al., 2021) and literature therein).

The behaviour of a supercooled liquid during the fast cooling that leads to the glass transition can be described by the melt fragility (m). This parameter represents the rate of the viscosity change as a function of the temperature near the glass transition temperature (T_g) (Angell, 1995). The fragility is defined as $m = \left[\partial \log \eta_l / \partial (T_g/T)\right]\big|_{T=T_g}$, where T_g is the temperature where $\eta_l(T_g) = 10^{12}$ Pa s. This parameter allows the distinction between *strong* glass forming liquids (having low m values) and *fragile* ones (having high m values).

Actually, m concerns the supercooled liquid but recent studies suggest that its value can be retrieved from the properties of the glass (Novikov and Sokolov, 2004; Scopigno et al., 2003), thus offering the possibility to parametrize the T-dependence of η_l without its direct measurement, once T_g is known. In particular, two key vibrational properties of volcanic glasses have been directly correlated with their parental melt fragility: (i) the ratio between the bulk (K) and the shear (G) moduli K/G, and (ii) the position of the boson peak (BP) maximum, a huge bump visible at low energy in the reduced vibrational density of states (VDoS) $g(E)/E^2$. These parameters can be obtained by means of Brillouin light scattering (BLS) and Raman spectroscopy (RS) (Cassetta et al., 2021), respectively.

Once known T_g, retrievable by differential scanning calorimetry (DSC), and m, derived via vibrational dynamics of glasses (Cassetta et al., 2021), η_l can be estimated with the MYEGA formalism that is based on the configurational entropy related to the topological constraint framework (Mauro et al., 2009). Such an approach showed its potential in several volcanic systems at different hydration level.

In this study, we focus our analysis on the RS-derived BP. Although its nature is still under debate, literature universally agrees that BP represents a fingerprint of the intrinsic disorder of glasses (Baldi et al., 2020; Chumakov et al., 2014; Schirmacher et al., 2007).

Among the variety of spectroscopic techniques used to measure the VDoS of silicate glasses (Berry et al., 2003; Bonnin-Mosbah et al., 2002; Mastelaro and Zanotto, 2018), RS combined with a microscope allows a space-resolved and non-invasive study of both their structural and chemical properties (Di Genova et al., 2015; Larre et al., 2020; Malfait et al., 2008; McMillan, 1989; Mysen et al., 1982).

The high-frequency (high-ω) region of the Raman spectra (800-1000 cm^{-1}) conveys information on the polymerization degree by the deconvolution of the Q^n species) (Di Muro et al., 2009; Mercier et al., 2009; Mysen et al., 1982). Conversely, an accurate analysis of the BP in the low-frequency spectral region (low-ω) region, below 150 cm^{-1}, allows the evaluation of the melt fragility of very small glass domains, also in highly crystallized samples.

Here, we provide a structural and rheological investigation in a set of residual basaltic-andesite glass obtained from dynamic crystallization experiments, as described in (Vetere et al., 2021). The analysis of the high-ω region of Raman spectra shows an increasingly polymerization degree of the residual glass which looks in contrast with that derived by the chemical composition.

On the other hand, we show the application of the spectroscopy-based model presented in (Cassetta et al., 2021) to estimate the residual melt viscosity starting from the glass obtained after the experimental quenching. To do that, we analysed the position of the BP maximum and we obtained the glass transition temperatures by DSC analysis. In addition, transmission electron microscopy

(TEM) and RS reveal the presence of iron-bearing nanocrystals, showing how these objects tie on the rheological evolution of such multiphase systems. Finally, we discuss both the analogies and differences with existing theoretical models in terms of viscosity evolution of our samples, as well as the advantages and limitations by using this approach.

Starting material, analytical and experimental methods

The investigated material is obtained from an andesitic rock erupted from Calbuco volcano (Chile), (Arzilli et al., 2019; Romero et al., 2016)) and a natural trachybasalt from 122 B.C. Plinian eruption of mount Etna (Italy), (Coltelli et al., 1998; Vetere and Holtz, 2021). The rheology of this material was investigated at high temperature and applied shear rate of 0.5 s^{-1} and 0.1 s^{-1} in order to shed new light on the occurrence of solid phases in these conditions (Vetere et al., 2021; Vetere and Holtz, 2021). Table 1 shows the chemical compositions of the basaltic-andesite and trachybasalt systems formed by a mixture of glasses and crystals as obtained by isothermal nucleation and growth experiment at 1473 K (samples E1, E2, E3, E4, and E5) and at 1493 K (samples E122 and E122rm, where the former is the starting glass while the latter is residual melt "rm" after the experiment). Moreover, we also includted two samples obtained by identical starting material (E1) but at different temperatures: sample E6 and E7 at 1483 and 1493 K, respectively (see Tab. 1). All experimental runs were quenched in air and then prepared for spectroscopic investigations by cutting and finally preparing a 200 μm-thick thin section.

	E1	E2	E3	E4	E5	E6	E7	E122	E122rm
SiO_2	56.50	56.44	56.33	58.34	58.78	57.91	56.27	49.41	50.53
TiO_2	0.92	0.95	0.95	1.16	1.18	1.06	1.00	1.72	1.98
Al_2O_3	18.22	18.27	18.35	16.10	15.59	17.46	18.04	18.81	17.38
FeO	7.45	7.56	7.70	7.99	6.84	6.51	7.09	9.53	10.89
MnO	0.15	0.15	0.15	0.18	0.18	0.12	0.12	-	-
MgO	4.13	4.01	3.75	4.60	4.93	4.27	4.13	3.58	4.13
CaO	7.91	7.93	7.97	6.96	6.66	7.23	8.04	9.23	8.61
Na_2O	3.90	3.88	4.02	3.37	4.89	4.25	4.18	4.15	4.40
K_2O	0.60	0.61	0.62	0.77	0.79	0.94	0.88	1.69	1.95
P_2O_5	0.22	0.20	0.16	0.17	0.17	0.26	0.24	-	-

Table 1. Residual glasses composition in wt.% of Calbuco experiments (E1-E7), (Vetere et al., 2021) and those of Etna 122 B.C. experiment (E122 and E122rm), (Vetere and Holtz, 2021).

Samples are multiphase systems and present small partly crystallized regions and large glassy domains. The dimension of the investigated glassy areas for each sample varies between 0.5 and 1 mm^2 and covers different part of the sample.

Due to the relatively large crystal fraction in sample E5, only residual glass domains with areas of about 10-20 μm^2 were taken into to account for the spectroscopic investigation.

Polarized HH (parallel) and HV (crossed) micro-Raman spectra were collected at room temperature on the glassy portions of thin sections. Measurement was done in back-scattering geometry with a Horiba-Jobin Yvon T-64000 triple-axis spectrometer used in a double subtractive configuration with three holographic gratings (1800 lines mm^{-1}). The spectrometer is equipped with a charge coupled device (CCD) detector (1024x256 pixels) cooled by liquid nitrogen allowing a spectral resolution of about 0.6 cm^{-1}/pixel. The light source is the 514.5 nm green line produced by a mixed Ar-Kr ion gas laser (Spectra Physics Satelite 2018 RM). The sampled glassy areas were selected by optically inspecting the samples through an Olympus microscope equipped with a 100x objective (numerical aperture NA = 0.90). Spectra were acquired with the same objective, focusing the laser beam onto a spot of ~1 μm. The laser power on the sample surface was set at 10 mW and no alteration of the sample surface due to laser irradiation were observed during the measurements. The subtraction of the background was done as described elsewhere (Cassetta et al., 2022). The micrometric spot size of this configuration allows to probe very small glass volumes in the residual glass domains without any possible interference due to crystals. The homogeneity of the glass in the domains was done by acquiring 5 spectra at different positions for each sample.

Samples E5 and E122rm were also investigated by TEM to check the morphological characteristics of the nanocrystals detected by RS. Samples were crushed in a zirconium ball mill and the obtained powder was dispersed in deionized water. The suspension was dropped onto carbon-formvar-coated copper grids and then dried overnight at room temperature. Images were acquired by using a transmission electron microscope Tecnai G2 Twin Spirit with 120 kV acceleration voltage.

DSC measurements were carried out using a thermogravimetric analyser coupled with simultaneous differential scanning calorimetry (TGA-DSC 3+, Mettler Toledo). Polished glass chips (40 to 80 mg) were carefully located in an alumina crucible, ensuring the maximum adhesion between the sample and crucible surface. A heating rate of 20 K min^{-1} under constant air flow rate of 100 mL min^{-1} was used in order to erase the thermal history of the sample up to 20 K above the glass transition interval. Afterward, samples were firstly cooled to 470 K and then heated at the same rate ($q_{c,h}$) up to 1020 K. To fulfil the enthalpy matching principle (Moynihan, 1995; Scherer, 1984), two rates were used, i.e. $q_{c,h}$ = 20 K min^{-1} first and then 10 K min^{-1}. The glass transition is thus defined by the onset temperature T_{onset}, i.e. the intersection between the tangents to the heat flow curve in the glassy state

and at the inflection point during the glass transition (see SI). When the sample experiences the glass transition with a heating rate of 10 K min^{-1}, a $\eta_l(T_{onset})\sim10^{12}$ Pa s is obtained (Scherer, 1984). Thus, T_{onset} measured at $q_{c,h}$ = 10 K min^{-1} can be considered the glass transition temperature T_g [$\eta_l(T_g)$ = 10^{12} Pa s] (Zheng et al., 2019).

Results and discussion

The high-frequency Raman spectra were evaluated by applying the correction for the temperature and the excitation line effects according to the Long expression (Long, 1977):

$$I(\omega) = I^{obs}\left\{\omega_0^3\ \omega\ \frac{[1 - \exp(-hc\omega/k_BT)]}{(\omega_0 - \omega)^4}\right\} \qquad (1)$$

where h is the Planck constant, k_B the Boltzmann constant, c the speed of light, T is the absolute temperature (in K), ω_0 the frequency of the incident laser light (514.5 nm, thus ω_0 = 19435.1 cm^{-1}), and ω the observed frequency (in cm^{-1}).

Figure 1 shows HH polarized Raman spectra of the residual glass of each sample between 250 and 1250 cm^{-1} which are characterized by the most significant silicate signature occurring in different frequency region: *i*) the R band (250-490 cm^{-1}) arising from the stretching of O atoms in 5, 6 -or higher- membered rings and *ii*) the D_1 and D_2 "defect" lines related to the breathing mode, corresponding to in-phase O-bending motion, of 4- and 3-fold (T) rings coordinated to both Al and Si atoms (Galeener, 1979; Le Losq et al., 2014; Umari and Pasquarello, 2003).

The spectrum profiles of samples E1, E2 and E3 do not show significant variations, as expected for the very similar chemical composition. Conversely, samples E4 and E5 show a remarkable increase of the D_1 band on the top of the R band. Variation in intensity suggests a different proportions between 4-, 3- and high-membered rings (Okuno et al., 2005). Thus, in E4, and even more in E5, D_1 intensity increase indicates probably a growing number of 4-membered rings.

In the glassy regions of sample E5, we observe a clear separation of D_2 as the residual glass composition is depleted in Al_2O_3 upon plagioclase crystallization mirroring perhaps a widening of the T-O-T angles (Le Losq et al., 2014). Finally, the weak band at 700-800 cm^{-1}, arising from the 3-fold degenerate "rigid cage" vibrational mode of SiO_4 units (Sen and Thorpe, 1977), or to T-O stretching vibrations in the T-O-T plane (Kalampounias et al., 2006), does not show appreciable spectral change among the samples. Notable exception is E5, where we detected the signature of magnetite nanocrystals (Di Genova et al., 2020) through their A_{1g} mode (Shebanova and Lazor, 2003)

peaked at about 660-670 cm^{-1} and marked with a star in Fig. 1. In Etna trachybasalt (E122), the higher iron content may produce a slight intensity increase of D_2 shoulder when compared to the Calbuco basaltic andesite, which although richer in silica presents an almost equivalent content of alumina.

Differences between the bulk E122 glass and the glass pools of its evolved counterpart E122rm, are much more evident. Magnetite signatures are systematically detected and turn out much more pronounced in E122rm with respect to E5. Concerning the differences of the pure glass structure (E122rm) can be observed a shift of the centroid in the high frequency region (850-1250 cm^{-1}). The low glass/crystal ratio allows the identification of the magnetite modes $E_g \sim 320$ cm^{-1} and the intense A_{1g}. However, glass signatures in the Raman spectra are intense enough to be analyzed. We also detected, although weakly, the presence of A_{1g} peak in quite isolated regions of E4 residual glass pools (Fig. S1).

TEM images of the glass pools nano-structure confirm the presence of these iron oxides nanocrystals, which are heterogeneously distributed within the glass. E5 nanolite size ranges between 10 and 50 nm as shown in Fig. 1, panel (b) and (c), while sample E122rm presents a large amount of small magnetite nanocrystals (about 5-20 nm) homogeneously distributed, confirming an improved crystallization tendency of the melt, as suggested by the RS.

Both Raman spectra analysis and the TEM images clearly indicate the presence of magnetite nanocrystals (Di Genova et al., 2020) with a measurable size/volume-fraction allowing us to extract specific information about the solid fraction content and shape (aspect ratio) detectable at the nanoscale. Following, it is also possible to recalculate the new chemical budget of the melt by indirectly infer on the depletion of chemical constituents belonging to the crystallized fraction.

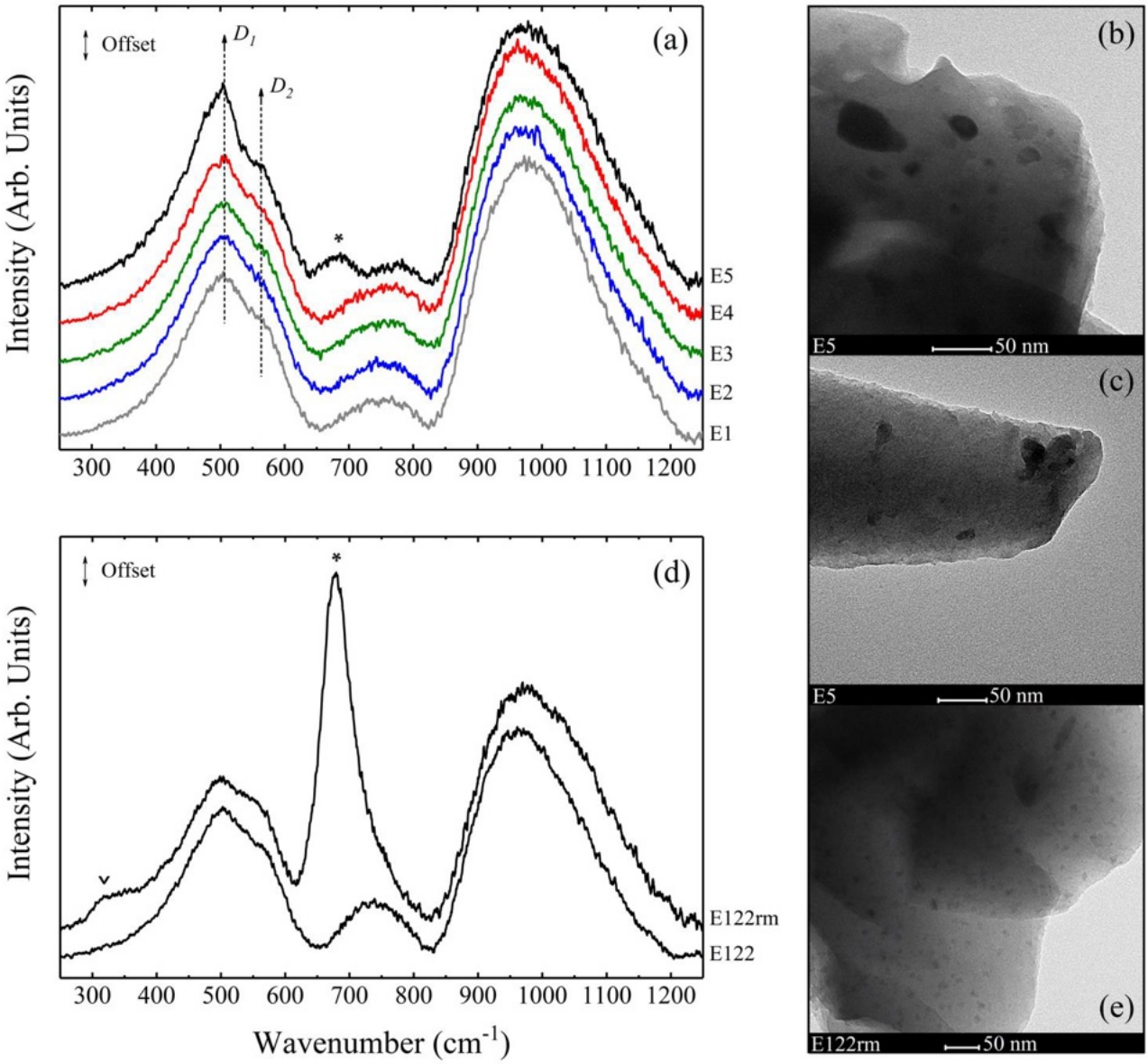

Figure 1. (a) HH polarized and Long-corrected spectra according to eq. 1. The spectra were probed in different pure glassy regions representing the mean residual melt of each run. Star indicates the centroid of the A_{1g} (a) and (d) sample E5 and E122rm and the E_g (v, E122rm) modes from the magnetite nanocrystals scattering, whilst the dashed arrow indicates the evolution of the D_1 band TEM images of E5 (b,c) and E122rm (e) glass pools fragments. The nanocrystals of magnetite dispersed in the glassy matrix ranges in size between 10-50 nm in E5 and 5 -20 nm in E122rm.

The high frequency (850–1250 cm^{-1}) region of silicate glasses exhibit vibrational modes of TO_4 tetrahedra and it is usually fitted (Mysen et al., 1982) by a set of spectral components related to the T-units, namely Q^n species, where n represents the number of bridging oxygens. The distribution of these species in glasses and melts is controlled by the chemistry χ of the sample (McMillan, 1984; Mysen et al., 1982). Thus, for a given number of bridging oxygens from 1 to 4, the different Q^n are termed Q^1, Q^2, Q^3, and Q^4, respectively, and their Gaussian-shaped bands are centered at about 960, 1070, 1100, and 1150 cm^{-1}, respectively (Mysen et al., 1982; Mysen, 1990). Frequency, area, and width of these spectral components mirror the polymerization degree of the glass, which is governed by the presence of network modifier (NM) cations and of charge balancing ones.

The deconvolution procedure has been carried out by constraining both the full width at half maximum (FWHM) and the frequency position of the Gaussian components to vary respectively within ±20 and ±5 cm^{-1} from the initially assigned values according to the procedure described in (Cassetta et al., 2022). Some approaches include 5 to 7 Gaussians, which are however limited to the analysis of polymerized systems (Di Genova et al., 2016; Di Muro et al., 2009; Stabile et al., 2021; Welsch et al., 2017). Conversely, our dataset presents systematically broad high frequency bells, typical of depolymerized basaltic glasses (Cassetta et al., 2022), in which is often difficult to clearly discriminate specific contributions that can be usually found in simple binary or ternary silicate systems (Le Losq and Neuville, 2017, 2013). Thus, we assigned the number of a bridging oxygen (1, 2, 3 and 4) to each Q^n unit and avoided to apply the splitting of the Q^4 band as suggested in (Le Losq et al., 2014) as well as the bimodal distribution of the Q^2 unit (Kilymis et al., 2019) and neglecting the T^{2S} as well as the Fe^{3+} band (Di Genova et al., 2017; Welsch et al., 2017).

Being aware that Raman bands have a non-gaussian nature (Cassetta et al., 2022; Malfait et al., 2008; Zotov et al., 1999), data interpretation is purely qualitative. Results of all the studied samples are reported in Tab. 2 and shown in Fig. 2, panels from (a) to (g).

In Calbuco experiments, the potential variations of Q^1 parameters (frequency position, area and full width at half maximum (FWHM)), as a function of the structural evolution, are not noticeable within the experimental uncertainty as well as those of Q^4, Q^2 fitting results show the lower values in sample E5 compared to the other samples. This difference is even more evident looking at the Q^3 distribution; in fact, relative areas and FWHM are slightly larger in sample E5. It is worth to note that Q^3 position (~1040 cm^{-1}) does not vary among samples.

The Etna 122 B.C. fitting results deliver a sharp increase of Q^4 relative area, accompanied by an equally decrease of Q^2 relative area. Conversely, frequency position and FWHM are not informative due to their large errors.

In the last panel of Fig. 2, is reported a first evaluation of the polymerization of the residual melts through a straightforward application of the ratio between the polymerizing units (Q^3+Q^4) and the depolymerizing ones (Q^1+Q^2) which can be expressed by a single parameter: (Q^3+Q^4)/(Q^1+Q^2) (Malchukova et al., 2018; Mysen, 1990). The trend shows an increase of the network polymerization by following the time evolution of the crystal nucleation and growth accompanied by an increasing SiO_2 content. The most evolved samples (E5 and E122rm) show the highest (Q^3+Q^4)/(Q^1+Q^2) ratio, highlighting the possibility that the melt is depleted in iron, through the Q^2 band intensity reduction (centered at ~960 cm^{-1}) as reported in Fig. 2 (e) and favoring the formation of iron bearing nanocrystals visible through its typical signature (see Fig. 1 (a) spectra E5). Regardless of the iron oxidation state and of which Raman band or Q^n unit can be related, the 960 cm^{-1} component (Di

Genova et al., 2020; Di Muro et al., 2009; Le Losq et al., 2019), its relative area reduction probably mirrors iron depletion which is observed to precipitate as nano-crystals in the glassy volume (see TEM images in Fig. 1 (b, c)).

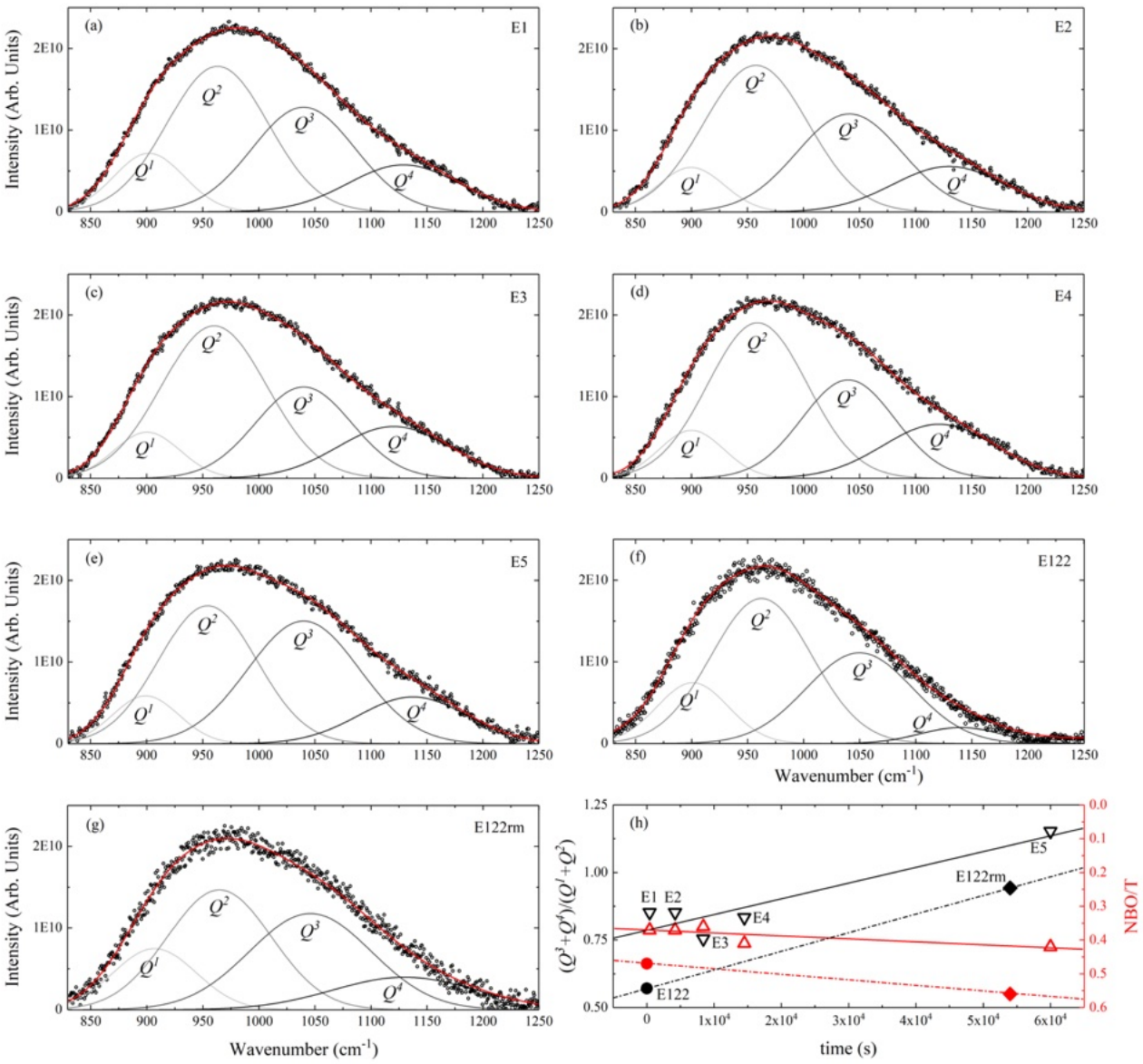

Figure 2. (a)-(g) deconvolution procedure of the high-frequency band of HH polarized Long-corrected Raman spectra. The red lines are the cumulative fitting curves from the Gaussian components Q^1, Q^2, Q^3, and Q^4 constrained as discussed in the text. (h) Relationship between $(Q^3+Q^4)/(Q^1+Q^2)$ ratio and experimental time, in red is reported the NBO/T value vs time in seconds (s).

	E1	E2	E3	E4	E5	E122	E122rm
Position (cm^{-1})							
Q^1	902 (2)	899 (1)	900 (1)	900 (2)	899 (1)	901 (3)	907 (4)
Q^2	963 (5)	957 (5)	960 (4)	959 (3)	954 (4)	962 (5)	964 (4)
Q^3	1040 (8)	1041 (4)	1040 (2)	1040 (2)	1040 (4)	1050 (6)	1046 (10)
Q^4	1129 (6)	1129 (8)	1120 (6)	1121 (5)	1137 (7)	1140 (6)	1130 (10)
Rel. area							
Q^1	0.12 (.04)	0.09 (.03)	0.09 (.02)	0.09 (.02)	0.09 (.03)	0.14 (.04)	0.15 (.05)
Q^2	0.42 (.05)	0.46 (.06)	0.48 (.05)	0.46 (.03)	0.38 (.03)	0.49 (.04)	0.37 (.05)
Q^3	0.31 (.04)	0.31 (.02)	0.26 (.03)	0.27 (.03)	0.39 (.04)	0.32 (.04)	0.35 (.05)
Q^4	0.15 (.03)	0.15 (.03)	0.17 (.02)	0.18 (.02)	0.14 (.03)	0.04 (.04)	0.14 (.06)
FWHM (cm^{-1})							
Q^1	73 (4)	69 (3)	69 (2)	68 (2)	69 (4)	75 (10)	87 (7)
Q^2	106 (12)	109 (4)	110 (2)	104 (6)	103 (7)	105 (6)	109 (10)
Q^3	108 (11)	111 (12)	101 (4)	97 (6)	117 (12)	112 (9)	128 (15)
Q^4	116 (5)	117 (6)	117 (3)	117 (4)	113 (6)	84 (4)	150 (10)

Table 2. Results from the Gaussian deconvolution: Raman shift (position in cm^{-1}); relative areas and full width at half maximum (FWHM in cm^{-1}). Errors are reported in brackets.

The study of the BP (Hehlen and Simon, 2012) is done by determining the position of its maximum as a function of the different samples, Fig. 3 (a). To isolate the low-ω signal of the BP, we carried out cross polarized HV measurement (Cassetta et al., 2022). This configuration suppresses the strong overlapping vibrations of 6-memberd rings from the R band tail at about 460 cm^{-1} (Le Losq et al., 2014).

As already mentioned, the BP is a feature in the reduced VDoS. Starting from the experimental Raman intensity $I^{obs}(\omega)$, the BP can be determined by calculating the reduced intensity $I^{red}(\omega)$. According to the Shuker and Gammon expression (Shuker and Gammon, 1970), for a Stokes process it is possible to state that:

$$I^{red}(\omega) = \frac{I^{obs}}{\omega\,[n(\omega,T)+1]} = C(\omega)\frac{g(\omega)}{\omega^2} \qquad (2)$$

where, $n(\omega,T)$ is the Bose-Einstein population factor, $n(\omega,T) = [\exp(\hbar\omega/k_BT)-1]^{-1}$, with k_B the Boltzmann constant, $\hbar$ the reduced Planck's one. The reduced Raman intensity $I^{red}(\omega)$ is proportional to the reduced VDoS $g(\omega)/\omega^2$ through the light-vibrations coupling function $C(\omega)$.

The BP position ω_{BP} was determined by fitting its shape to a log-normal function (Malinovsky et al., 1991) as described in (Cassetta et al., 2021). The maximum ω_{BP} shifts from 71.5 cm^{-1} (E1) to 65.9 (E5) and it was found to be close to 72 cm^{-1} in E122 and 63 cm^{-1} in the residual glass pools of its evolved counterpart (E122rm). The trend follows the gradual SiO_2 enrichment in the residual liquid and similarly seems to contradict the polymerization degree expressed by the NBO/T parameter. Considering the chemical data provided in Tab. 1 the E1-E5 NBO/T values range from 0.37 to 0.42, suggesting a depolymerization of Calbuco residual melts during time. TEM images and Raman results show the presence of nanocrystals. Thus, EPMA data on E4 (probably since they are very poorly detected), E5 and E122rm do not reproduce only the residual glass but glass plus nanolites (due to the relatively large spot used for analysis). Considering also that nanolite are mainly magnetite ($Fe^{2+}Fe^{3+}{}_2O_4$) and taking into account the crystallized volume (~ 3 vol%), the iron content into the residual melts is depleted by ~ 4 wt%. Considering the corrected Fe content (obtained by the removal of ~ 4 wt%. $FeO_{(t)}$ assuming $Fe^{3+}/FeO_{(t)}$ ~ 0.7 as per (Prata et al., 2019)) into the residual melts the recalculated NBO/T validates the $(Q^3+Q^4)/(Q^1+Q^2)$ ratio evolution thus showing an inverse correlation with the Raman-derived polymerization degree.

Indeed, polymerization index expressed by the Q^n species $(Q^3+Q^4)/(Q^1+Q^2)$ is in line with NBO/T data. This result also suggests an evolving melt toward a strong liquid and a more polymerized structure with, for instance, a decreasing bulk modulus (Cassetta et al., 2021).

The BP intensity does not show appreciable variation in samples E1, E2, E3 and E4, whereas in E5 it notably increases. The BP shift is much more evident when observing the case of E122 glass, where the shift is ~ 9 cm^{-1}. The BP evolution was evaluated through the squeezed frequency $v = \omega/\omega_{BP}$ by performing the variable transformation $g(v)dv = g(\omega)d\omega$. According to (Fontana et al., 2007, 1999), we assumed $C(\omega) \propto \omega$ in the BP region. Thus, the rescaled intensity can be rewritten as:

$$I^{red}(v) = I^{red}(\omega)\ \omega_{BP}^2 \qquad (3)$$

The $I^{red}(v)$ spectra are reported in Fig. 3(b), where can be observed a good scaling for E1, E2, E3 and E5 low-frequency spectra, whilst E4 drops slightly the master curve turning out whit a lower $I^{red}(v)$. Disagreement in the scaling procedure between the BP maximum shift and its intensity is usually ascribed to a different role played by the local structure of the glass (Ando et al., 2021; Orsingher et al., 2010; Zanatta et al., 2011). In our case, sample E4 intensity differs <10% with respect to the master curve. This result probably indicates a marginal structural reorganization within the glass

network in the probed region (see (Cassetta et al., 2022) and reference therein). Similarly, the scaling procedure of the Etna glasses works well in the BP maxima region. Moving to the higher frequency of the E122rm scaled spectra, we observe a broadening of its tail. This little excess that could be ascribed to a different distribution of the VDOS. These results suggest an overall hardening of the elastic medium of the carrying phase during time. In particular, the existence of the master curves (in both cases) underpins that the residual glass roughly maintains the same microscopic configuration, although its macroscopic properties changes (Cassetta et al., 2022; Zanatta et al., 2010).

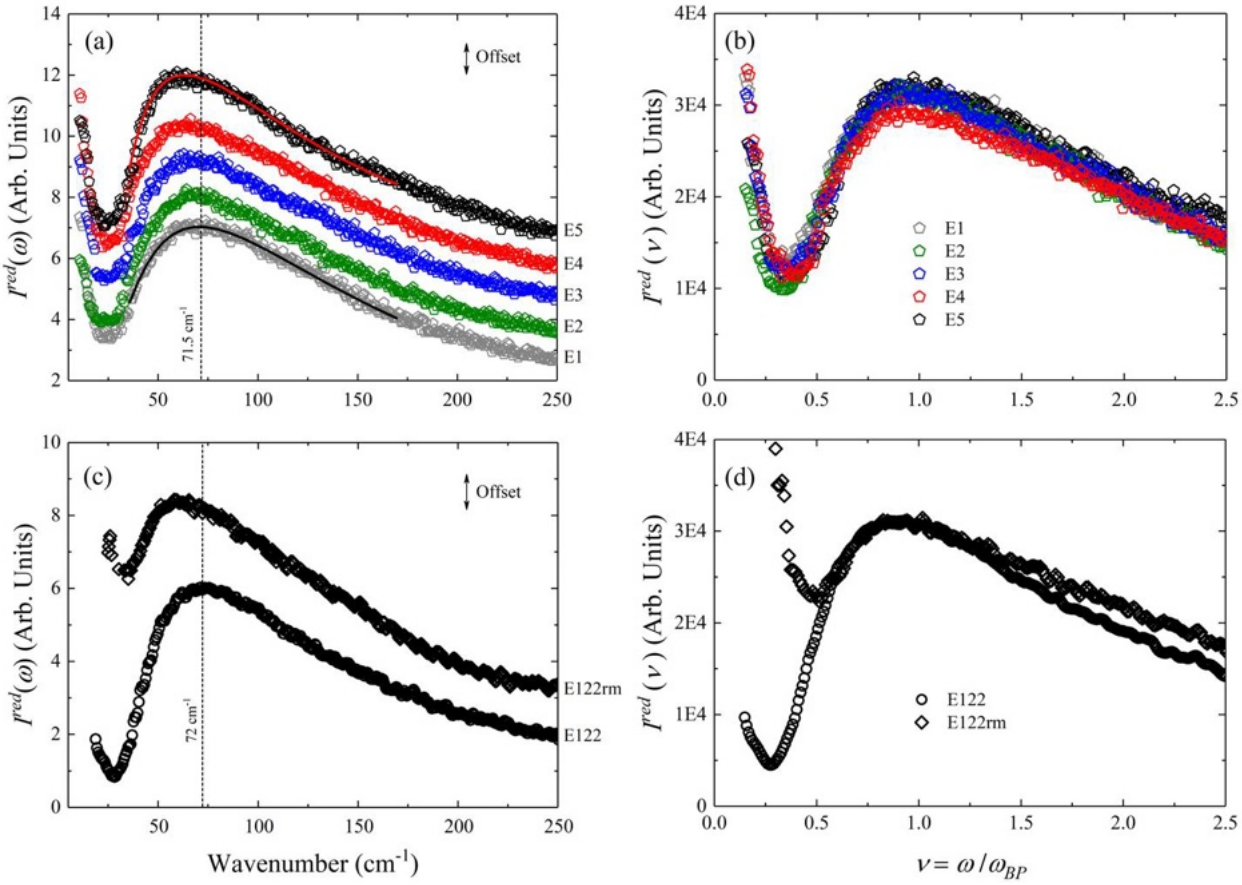

Figure 3. (a) Reduced low-frequency HV Raman spectra of E1, E2, E3, E4 and E5 residual glasses, after the subtraction of the rotational modes of air and those of Etna 122 in (c). The black and the red lines provide an example of the log-normal function used for the fitting procedure in the form of $I(\omega) \propto \exp\{-[\ln(\omega/\omega_{BP})]^2/2\sigma^2\}$, where σ is the BP width and ω_{BP} its position in cm^{-1}. The black dashed lines refer to the ω_{BP} of sample E1 and E122 respectively. Scaling procedure according to eq. 3 for the Calbuco (b) and Etna 122 B.C. (d) glass pools.

In order to investigate the effect of the glass vibrational-derived melt viscosity, it is important to recall some aspects discussed in (Cassetta et al., 2021). *i*) It must be assumed that the vibrational dynamics of glasses embed the melt fragility (Novikov and Sokolov, 2004; Scopigno et al., 2003). *ii*) The model is built on the MYEGA formalism formulated by (Mauro et al., 2009). Here, the high-temperature viscosity limit of silicate liquids of the MYEGA model was set at $10^{-2.93}$ Pa s (based on the analysis of 946 curves) representing a universal parameter (Zheng et al., 2011). Thus, the only

two independent parameters controlling the T-dependence of viscosity are the T_g and m. This assumption simplifies *the modeling process of the compositional dependence of viscosity* (Zheng et al., 2011) since the thermodynamic quantities defined in the MYEGA formalism roots on the minima energy-landscape analysis of (Stillinger, 1988) and on the topological constraint theory (Phillips, 1979). This approach is particularly effective in describing the phase diagrams of thermal, kinetic, vibrational, and other physical properties of several network glasses, with particular regard to the glass transition interval (Boolchand et al., 2005).

Using the model of (Cassetta et al., 2021), the melt fragility (m) can be estimated from the BP frequency position of the glass pools, as follow:

$$m = 1.7 \exp (\omega_{BP}/28) + 14.97 \quad (4)$$

Considering the method introduced by (Zheng et al., 2020) and readapted for volcanic glasses by (Di Genova et al., 2020), the low-temperature viscosity data and T_g can be retrieved via DSC approach by exploiting the relation between fictive temperatures (T_f), $q_{c,h}$ and viscosity. Thermograms with different $q_{c,h}$, were used to determine the shift factors as reported by (Di Genova et al., 2020) in order to retrieve the viscosity at a given temperature:

$$\log \eta_l (T_{onset,\ peak,\ end}) = K_{onset,\ peak,\ end} - \log (\left| q_{c,h} \right|) \quad (5)$$

Here $q_{c,h}$ stands for heating-cooling rates at which the $T_{onset,}$ $T_{peak,}$ T_{end} were measured, while $K_{onset,}$ $K_{peak,}$ K_{end} are the chemically-independent parallel shift factors. DSC signals of partly crystallized melts (i.e. E4, E5 and E122rm) provided evaluable signals only for $q_{c,h}$ = 20 K min^{-1}. However, the trend of log η_l over $10^4/T$ can be assumed to be Arrhenius within the low T-interval (1020-870 K) allowing a linear interpolation considering the T_g at log η_l = 12. The Calbuco sample E1 has a T_{onset} = 939 K, a T_{peak} = 978 K and a T_{end} = 993 K when applied q_c = 10 K min^{-1}, whilst with a q_c = 20 K min^{-1}, T_{onset} = 947 K and T_{peak} = 988 K. This provides viscosity value of ~ 10^{12}, $10^{10.61}$, $10^{9.98}$, $10^{10.55}$, $10^{10.02}$ and $10^{9.68}$ Pa s, respectively.

Samples E4 and E5 provided good DSC signals only by applying q_c = 20 K min^{-1}. Therefore, E4 shows T_{onset}, T_{peak} and T_{end} at 949, 991 and at 1020 K, respectively, whilst for E5 was only possible to get obtain T_{onset} and T_{peak} at 954 and 997 K, respectively. The weakness of the heat flow signal in sample E5 is probably due to the small glass fraction available (15 mg). By using a q_c = 10 K min^{-1}, E122 sample shows T_{onset}, T_{peak} and T_{end} at 916, 960 and 985 K, respectively. In analogy with E4 and

E5, the sample E122rm shows reliable T_{onset}, T_{peak} and T_{end} with a q_c = 20 K min^{-1} at 938, 975 and 1000 K (thermograms are reported in Fig. S3).

By using eq. 5 we obtained the DSC-derived viscosity data reported in Fig. 4 (a and b) for Calbuco and Etna volcanoes, respectively. Afterwards, we derived the T_g from the interpolation of the viscosity points calculated with q_c = 20 K min^{-1}.

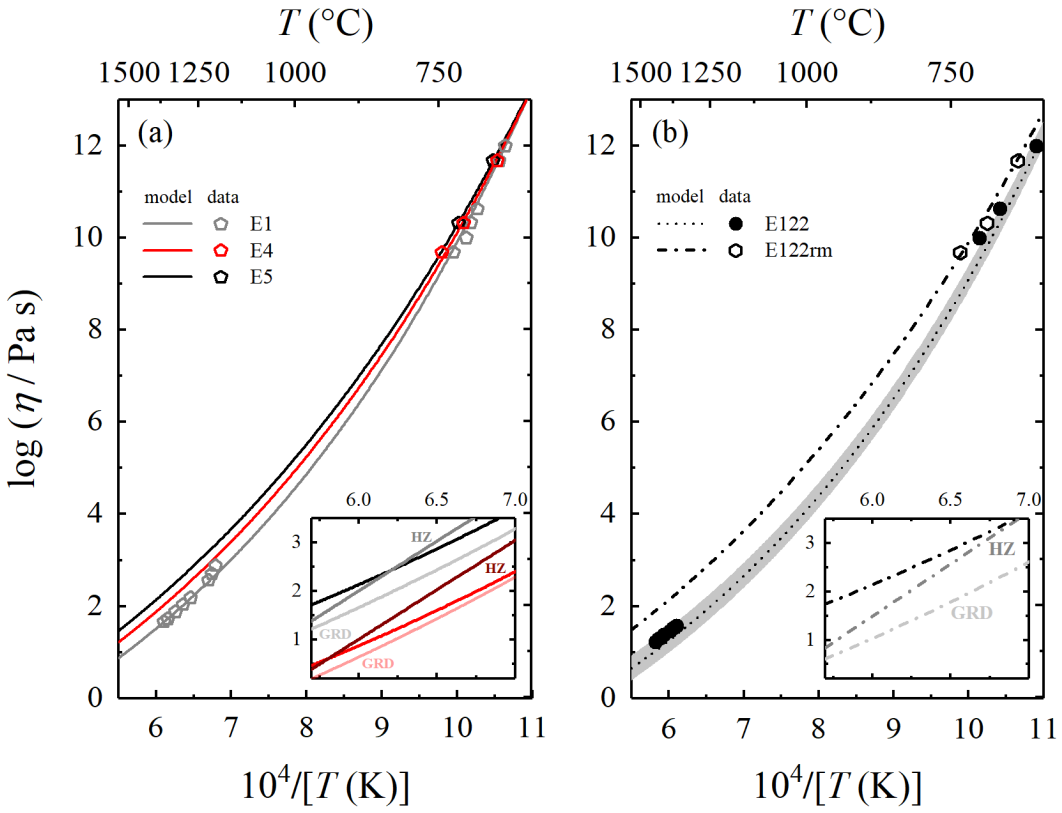

Figure 4. (a) Measured low-viscosities by concentric cylinders of a Calbuco andesite (grey symbols, data provided by (Vetere et al., 2021; Vetere and Holtz, 2021)) and DSC-derived high-viscosity data of E1, E4 and E5. Solid lines represent the MYEGA curves obtained by combining the BP-derived m and T_g estimated as explained in the text. (b) Measured low-viscosities by concentric cylinder (solid black dots, data provided by (Vetere and Holtz, 2021)) and DSC-derived high viscosity data of E122 and E122rm with BP-derived viscosity MYEGA curves depicted by the dotted and dash-dotted lines respectively. Grey area is the accuracy of the model (0.27 log units). The insets in (a) and (b) report the plot of the high-temperature predictions from empirical models of (Hui and Zhang, 2007) (HZ) and (Giordano et al., 2008) (GRD). For sake of clarity predictions for E4 are in the inset in (a) are shifted of -1 log η.

The obtained fragility values (calculated by eq. 4) for E1-E5 glasses are 36.8, 36.1, 35.7, 34.2 and 32.9, respectively, whilst those of Etna 122 are 37.2 and 31.01 for the starting material E122 and the post-run experiment E122rm respectively. The calculated melt viscosity values (by replacing the measured T_g in eq. 4) at T = 1473 K ranges from 2.67 to 3.33 log units for the Calbuco basaltic-andesite, and from 2.20 to 3.16 log units for the Etna 122 B.C.

The MYEGA curves with m, T_g and $\eta_\infty = 10^{-2.93}$, describing the temperature dependence of the residual melt viscosity of our samples, are reported in Fig. 4 (a) and (b). The high temperature lines

obtained from (Cassetta et al., 2021), show intersections with the HZ model (Hui and Zhang, 2007) and considerable divergences mainly in samples E4 and E122rm, unlike the GRD model (Giordano et al., 2008) which provides systematically lower values (1 order of magnitude in E122rm) and similar slope, with the exception of E4 showing quite similar values.

The derived viscosity-temperature trend is in line with both low- and high-viscosity experimental data in the case of the E1 (Calbuco starting material, Fig. 4 (a)), and slightly below the measured η_l for sample E122 (Fig. 4 (b)). For the latter, our prediction lies within the model accuracy (0.27 log units (Cassetta et al., 2021)), which is shown as the grey region in Fig. 4 (b) surrounding the model curve. BP results and calculated η_r^{BP} are reported in Tab. 3 for the whole set of samples. By using an identical approach, we have calculated the melt fragility values derived from experiments performed at 1483 and 1493 K, respectively, named E6 and E7 (Tab. 3).

	ω_{BP} (cm^{-1})	m	T_g (K)	Φ_{tot} (area %)	AS mean	η_{app} (Pa s)	η_l^{BP} (Pa s)	η_l^{Grd} (Pa s)	η_r^{BP}	η_r^{Liu}	η_r^{Mdr}
E1	71.5 (.6)	36.8	939	0	-	$10^{2.88}$	$10^{2.67}$	$10^{2.75}$	-	-	-
E2	70.6 (.3)	36.1	-	0	-	$10^{2.92}$	$10^{2.77}$	$10^{2.76}$	-	-	-
E3	70.1 (.4)	35.7	-	1	6.0	$10^{3.15}$	$10^{2.82}$	$10^{2.77}$	2.13	1.07	1.05
E4	68.0 (.3)	34.2	942	22	7.0	$10^{3.59}$	$10^{3.05}$	$10^{2.91}$	3.31	10.01	6.05
E5	65.9 (.4)	32.9	945	25	8.1	$10^{3.88}$	$10^{3.33}$	$10^{2.92}$	3.55	16.07	13.08
E6	68.0 (.4)	34.2	-	13	6.7	$10^{3.62}$	-	$10^{2.89}$	3.49	3.10	2.24
E7	69.2 (.3)	35.1	-	6	9.9	$10^{3.14}$	-	$10^{2.62}$	2.23	2.00	1.48
E122	72.0 (1)	37.2	915	0	-		$10^{2.20}$	$10^{2.13}$	-	-	-
E122rm	63 (1)	31.1	924	21	7.0	$10^{3.81}$	$10^{3.16}$	$10^{2.10}$	4.21	12.70	6.52

Table 3. Boson peak (BP) frequencies (ω_{BP}) of the glass pools (errors reported in brackets), BP-derived m, the measured T_g (with an accuracy of ± 1K), crystal fraction in area % (Φ_{tot}) and apparent viscosities η_{app} provided by (Vetere et al., 2021), BP liquid (η_l^{BP} ± 0.27 log units) and relative (η_r^{BP}) viscosities obtained as explained in the text and relative viscosities derived by using the η_l from the model of (Giordano et al., 2008) (η_r^{Grd}) and those derived from the models of (Liu et al., 2017; Mader et al., 2013), (η_r^{Mdr}, η_r^{Liu}).

The increase of the DSC-derived viscosities is caused by chemical modification of the residual melt: iron depletion due to the crystallization of magnetite even though EMPA shows slight increase of SiO_2 (~ 2%) and a removal of CaO (~ 1%) and Al_2O_3 (~ 2.5%) during the crystallization of plagioclase. Such effect is largely observed in literature (Di Genova et al., 2020; Fotheringham et al., 2011). This behavior is weaker for the Calbuco basaltic-andesite while the Etna 122 trachybasalt shows a larger viscosity increase. From the rheological point of view, DSC-derived final viscosity runs (E122rm) are much higher if compared to the final one of the Calbuco (E5) due to the high nanolites content as previously shown by TEM and Raman analysis.

433 It is worth to highlight that we obtained similar values of the BP-derived *m* parameters as those
434 reported in (Cassetta et al., 2021) for the andesite sample MSA (slightly enriched in SiO_2 and Al_2O_3
435 with a ω_{BP} = 66.5 cm^{-1} and *m* = 33.2), as well as with the MYEGA-*m* derived by fitting the viscosity
436 data of andesite with similar composition from (Neuville et al., 1993). Our results are also in line with
437 an iron-free andesitic melt (Richet et al., 1996) having *m* = 36.2 and a similar chemical NBO/T index
438 of our starting material. Conversely, our liquid viscosity derived data are slightly higher (within the
439 experimental accuracy) than those chemically estimated for E2 and E3, whilst the difference increases
440 of about 0.2 log units for E4 and 0.4 log units for E5. The vibrational derived viscosities and the
441 apparent viscosities show very similar trends, which are in agreement with the expected viscosities
442 at Φ = 0 (E1 and E2) and Φ = 1 (E3), being $\eta_l \sim \eta_{app}$. For larger crystal fraction, as the time of the
443 experimental run increases, we observe $\eta_l << \eta_{app}$ at Φ > 22% (E4 and E5).
444 Our results are also consistent with the observed low-viscosity data by considering 3
445 measurements at 3 different temperatures (E1, E6 and E7 at 1473, 1483 and 1493 K, respectively)
446 and a further dataset of a similar andesite from the Calbuco volcano having a slightly different
447 chemical composition; data are provided by (Vetere and Holtz, 2021) and shown in Fig. 4 (a). This
448 result is in line with those found in (Vetere et al., 2021) thereby confirming the model (Cassetta et
449 al., 2021) as an efficient tool to estimate the liquid viscosity of the residual melt pools.
450 The calculated η_r values with the ω_{BP}-derived η_l of the isothermal runs at 1473 K are reported
451 in Tab. 3. In addition, we included samples E6 and E7 to further evaluate the effect of varying Φ on
452 *m* (the reduced low-ω Raman spectra of glass pools of samples E6 and E7 are reported in Fig. S2,
453 whilst their ω_{BP} in Tab. 3). The obtained results and their relationship with the total crystallinity Φ_{tot}
454 are reported in Tab. 3.
455 Comparing η_r obtained by the η_l estimated from the χ-based model of (Giordano et al., 2008)
456 and η_{app} from experimental approach of (Vetere et al., 2021), we obtain an underestimated value for
457 E3 (Φ = 1%) of about 1.2. Mostly, the η_r values and those derived by multiphase rheological model
458 of (Liu et al., 2017; Mader et al., 2013) show a good agreement as the crystallinity ranges $1 \leq \Phi \leq$
459 13. Higher Φ values ($\Phi \geq 22\%$) result in lower η_r values. In particular, we found a mismatch of about
460 2.74 (E4) and 9.53 (E5) with the model of (Mader et al., 2013), whilst 6.7 and 21.7 units with those
461 derived by the model of (Liu et al., 2017). Similar behavior has been highlighted by (Del Gaudio et
462 al., 2013) for Φ > 20 %.
463 The η_r variations mentioned above may be dictated by the estimated χ (and, as consequence
464 melt viscosity when using literature models such as (Giordano et al., 2008)) which is limited in a
465 relatively large area of probing using EMPA compared with our approach. The fact that residual melts

in partly crystallized systems could contain non-detectable nanosized crystals that may lead to an underestimation of the η_l due to FeO_t depletion. This could be largely the case for E5 and E122rm (and marginally for E4) experiments, since we found evidence of an increasingly polymerizing structure of the glass pools in the high-frequency Raman spectra, expressed by the parameter $(Q^3+Q^4)/(Q^1+Q^2)$, concomitantly with the magnetite nanocrystalline signature revealed through the 690 cm^{-1} band (Fig. 1 (a) and (d)), spectra E5 and E122rm and confirmed by TEM analysis, Fig. 1 (b), (c) and (e). It is worth to note that modification of the melt structure, with formation of high-η shells surrounding magnetite crystals, and possible aggregation that effectively increase Φ, compete all together to increase the viscosity (Bouhifd et al., 2004; Di Genova et al., 2020).

Moreover, the influence of different amount and size of spherically-occurring nanocrystals strongly influence the η_r Φ-dependence curves as shown elsewhere (Del Gaudio et al., 2013; Di Genova et al., 2020). As a matter of fact, nucleation of magnetite strongly lowers the used AS and the maximum packing fraction (Φ_m). Moreover, detection limit of scanning electron microscope images may also reduce the observable number of particles detectable in determining the Φ_{tot}, for instance, while estimating the relative viscosities via multiphase rheological models (see (Liu et al., 2018) and literature therein).

Conclusions

This study assessed the potentialities of micro-Raman investigation and analysis in representing the rheological change of evolving silicate liquids. The MYEGA formalism, which is based on the topological model for the configurational entropy, allows a realistic determination of η_l. We show that micro-RS offers a crucial tool in evaluating the melt fragility m through the BP position ω_{BP} from low-ω HV spectra. The interdependency of the low- and high-ω regions of HV and HH Raman spectra, improve significantly the evaluation of the melt structure enabling a through parametrization of the polymerization degree.

The present study points to further understanding of volcanologically relevant multiphase systems by empirical observations marked by an increasing spatial resolution in investigating quite small glass areas (i.e. highly crystalline sample). In general, deformation applied to silicate melts enhances nucleation and growth rates. Residual glasses investigated by RS and TEM show the presence of nanolites that could not be detected using only EPMA approach. As a consequence, if nanolites are volumetrically relevant, residual melts chemical data could induce to an underestimation of the polymerization degree (NBO/T) and inevitably the residual melt viscosity. Therefore, nanolites could

drastically influence rheology of partially crystallized silicate melts and this point needs to be considered in modeling magmatic and volcanic behaviors and risks managements in volcanic areas.

Acknowledgements

The authors warmly acknowledge Erika Lorenzetto and Marco Giarola (Technological Platform Center, CPT) of the University of Verona for the TEM images and the precious support during micro-Raman measurements, respectively, and prof. Gino Mariotto for the skillful advices and discussions. Detailed and useful comments by the Editor and two anonymous reviewers improved the final version of this study. MC thanks Gianni Versiglioni for all the support termed "*luce*".

References

Ando, M.F., Fuhrmann, S., Pan, Z., Rodrigues, B.P., Mori, T., Ebbinghaus, S.G., Wondraczek, K., Kitani, S., Wondraczek, L., 2021. Boson peak and structural heterogeneity in ternary SiO_2-Al_2O_3-B_2O_3 glasses. J. Am. Ceram. Soc. 1–10.

Angell, C.A., 1995. Formation of glasses from liquids and biopolymers. Science 267, 1924–1935.

Arzilli, F., Morgavi, D., Petrelli, M., Polacci, M., Burton, M., Di Genova, D., Spina, L., La Spina, G., Hartley, M.E., Romero, J.E., Fellowes, J., Diaz-Alvarado, J., Perugini, D., 2019. The unexpected explosive sub-Plinian eruption of Calbuco volcano (22–23 April 2015; southern Chile): Triggering mechanism implications. J. Volcanol. Geotherm. Res. 378, 35–50.

Baldi, G., Fontana, A., Monaco, G., 2020. Vibrational dynamics of non-crystalline solids. ArXiv 2011, 10415.

Berry, A.J., O'Neill, H.S.C., Jayasuriya, K.D., Campbell, S.J., Foran, G.J., 2003. XANES calibrations for the oxidation state of iron in a silicate glass. Am. Min. 88, 967–977.

Bonnin-Mosbah, M., Métrich, N., Susini, J., Salomé, M., Massare, D., Menez, B., 2002. Micro X-ray absorption near edge structure at the sulfur and iron K-edges in natural silicate glasses. Spectrochim. Acta. Part. B At. Spectrosc. 57, 711–725.

Boolchand, P., Lucovsky, G., Phillips, J.C., Thorpe, M.F., 2005. Self-organization and the physics of glassy networks. Philos. Mag. 85, 3823–3838.

Bouhifd, M.A., Richet, P., Besson, P., Roskosz, M., Ingrin, J., 2004. Redox state, microstructure and viscosity of a partially crystallized basalt melt. Earth. Planet. Sci. Lett. 218, 31–44.

Caricchi, L., Burlini, L., Ulmer, P., Gerya, T., Vassalli, M., Papale, P., 2007. Non-Newtonian rheology of crystal-bearing magmas and implications for magma ascent dynamics. Earth. Planet. Sci. Lett. 264, 402–419.

Cassetta, M., Di Genova, D., Zanatta, M., Boffa Ballaran, T., Kurnosov, A., Giarola, M., Mariotto, G., 2021. Estimating the viscosity of volcanic melts from the vibrational properties of their parental glasses. Sci. Rep. 11, 13072.

Cassetta, M., Zanatta, M., Biesuz, M., Giarola, M., Mariotto, G., 2022. New insights about the role of Na–K ratio on the vibrational dynamics of synthetic- basalt glasses. J. Raman Spectrosc. 1–10.

Chumakov, A.I., Monaco, G., Fontana, A., Bosak, A., Hermann, R.P., Bessas, D., Wehinger, B., Crichton, W.A., Krisch, M., Rüffer, R., Baldi, G., Carini, G., Carini, G., D'Angelo, G., Gilioli, E., Tripodo, G., Zanatta, M., Winkler, B., Milman, V., Refson, K., Dove, M.T., Dubrovinskaia,

N., Dubrovinsky, L., Keding, R., Yue, Y.Z., 2014. Role of disorder in the thermodynamics and atomic dynamics of glasses. Phys. Rev. Lett. 112, 1–6.
Coltelli, M., Del Carlo, P., Vezzoli, L., 1998. Discovery of a Plinian basaltic eruption of Roman age at Etna volcano, Italy. Geology 26, 1095–1098.
Del Gaudio, P., Ventura, G., Taddeucci, J., 2013. The effect of particle size on the rheology of liquid-solid mixtures with application to lava flows: Results from analogue experiments. Geochem. Geophys. Geosyst. 14, 2661–2669.
Di Genova, D., Brooker, R.A., Mader, H., Drewitt, J.W.E., Longo, A., Deubener, J., Neuville, D.R., Fanara, S., Shebanova, O., Anzellini, S., Arzilli, F., Bamber, E.C., Hennet, L., La Spina, G., Miyajima, N., 2020. In situ observation of nanolite growth in volcanic melt: A driving force for explosive eruptions. Sci. Adv. 6, 1–13.
Di Genova, D., Hess, K.U., Chevrel, M.O., Dingwell, D.B., 2016. Models for the estimation of Fe^{3+}/Fe_{tot} ratio in terrestrial and extraterrestrial alkali- and iron-rich silicate glasses using Raman spectroscopy. Am. Min. 101, 943–952.
Di Genova, D., Morgavi, D., Hess, K.-U., Neuville, D.R., Borovkov, N., Dingwell, D.B., 2015. Approximate chemical analysis of volcanic glasses using Raman spectroscopy. J. Raman Spectrosc. 46, 1235–1244.
Di Genova, D., Vasseur, J., Hess, K.U., Neuville, D.R., Dingwell, D.B., 2017. Effect of oxygen fugacity on the glass transition, viscosity and structure of silica- and iron-rich magmatic melts. J. Non Cryst. Solids 470, 78–85.
Di Genova, D., Zandona, A., Deubener, J., 2020. Unravelling the effect of nano-heterogeneity on the viscosity of silicate melts: implications for glass manufacturing and volcanic eruptions. J. Non Cryst. Solids. 545, 120248
Di Muro, A., Métrich, N., Mercier, M., Giordano, D., Massare, D., Montagnac, G., 2009. Micro-Raman determination of iron redox state in dry natural glasses: Application to peralkaline rhyolites and basalts. Chem. Geol. 259, 78–88.
Dingwell, D.B., 1996. Volcanic dilemma: Flow or blow? Science 273, 1054–1055.
Dingwell, D.B., Hess, K.-U., Romano, C., 1998. Extremely fluid behavior of hydrous peralkaline rhyolites. Earth Planet Sci. Lett. 158, 31–38.
Fontana, A., Dell'Anna, R., Montagna, M., Rossi, F., Viliani, G., Ruocco, G., Sampoli, M., Buchenau, U., Wischnewski, A., 1999. The Raman coupling function in amorphous silica and the nature of the long-wavelength excitations in disordered systems. Europhys Lett. 47, 56–62.
Fontana, A., Rossi, F., Viliani, G., Caponi, S., Fabiani, E., Baldi, G., Ruocco, G., Dal Maschio, R., 2007. The Raman coupling function in disordered solids: A light and neutron scattering study on glasses of different fragility. J. Phys. Condens. Matter 19, 205145.
Fotheringham, U., Wurth, R., Rüssel, C., 2011. Thermal analyses to assess diffusion kinetics in the nano-sized interspaces between the growing crystals of a glass ceramics. Thermochim. Acta 522, 144–150.
Galeener, F.L., 1979. Band limits and the vibrational spectra of tetrahedral glasses. Phys. Rev. B 19, 4292–4297.
Giordano, D., Russell, J.K., Dingwell, D.B., 2008. Viscosity of magmatic liquids: A model. Earth Planet. Sci. Lett. 271, 123–134.
Gonnermann, H.M., Manga, M., 2007. The Fluid Mechanics Inside a Volcano. Annu. Rev. Fluid Mech. 39, 321–356.
Hehlen, B., Simon, G., 2012. The vibrations of vitreous silica observed in hyper-Raman scattering. J. Raman Spectrosc. 43, 1941–1950.
Hui, H., Zhang, Y., 2007. Toward a general viscosity equation for natural anhydrous and hydrous silicate melts. Geochim. Cosmochim. Acta 71, 403–416.
Kilymis, D., Ispas, S., Hehlen, B., Peuget, S., Delaye, J.-M., 2019. Vibrational properties of sodosilicate glasses from first-principles calculations. Phys. Rev. B 99.

595 Kolzenburg, S., Hess, K.U., Berlo, K., Dingwell, D.B., 2020. Disequilibrium Rheology and
596 Crystallization Kinetics of Basalts and Implications for the Phlegrean Volcanic District. Front.
597 Earth. Sci. (Lausanne) 8.
598 Larre, C., Morizet, Y., Bézos, A., Guivel, C., La, C., Mangold, N., 2020. Particular H_2O dissolution
599 mechanism in iron-rich melt: Application to martian basaltic melt genesis. J. Raman Spectrosc.
600 51, 493–507.
601 Le Losq, C., Neuville, D.R., 2017. Molecular structure, configurational entropy and viscosity of
602 silicate melts: Link through the Adam and Gibbs theory of viscous flow. J. Non Cryst. Solids
603 463, 175–188.
604 Le Losq, C., Neuville, D.R., 2013. Effect of the Na/K mixing on the structure and the rheology of
605 tectosilicate silica-rich melts. Chem. Geol. 346, 57–71.
606 Le Losq, C., Neuville, D.R., Florian, P., Henderson, G.S., Massiot, D., 2014. The role of Al^{3+} on
607 rheology and structural changes in sodium silicate and aluminosilicate glasses and melts.
608 Geochim. Cosmochim. Acta 126, 495–517.
609 Le Losq, C. le, Berry, A.J., Kendrick, M.A., Neuville, D.R., O'Neill, H.S.C., 2019. Determination
610 of the oxidation state of iron in Mid-Ocean Ridge basalt glasses by Raman spectroscopy. Am.
611 Min. 104, 1032–1042.
612 Liu, Z., Blanpain, B., Guo, M., 2017. Viscosity of Heterogeneous Silicate Melts: A Non-Newtonian
613 Model. Metal. Mat. Trans. B 48, 3027–3037.
614 Liu, Z., Pandelaers, L., Blanpain, B., Guo, M., 2018. Viscosity of Heterogeneous Silicate Melts: A
615 Review. Metal. Mat. Trans. 49, 2469–2486.
616 Long, D.A., 1977. Raman Spectroscopy, I. ed. McGraw-Hill Book, New York.
617 Mader, H.M., Llewellin, E.W., Mueller, S.P., 2013. The rheology of two-phase magmas: A review
618 and analysis. J. Volcanol. Geotherm. 257, 135–158
619 Malchukova, E. V., Nepomnyashchikh, A.I., Boizot, B., Terukov, E.I., 2018. Radiation Effects and
620 Optical Properties of Aluminoborosilicate Glass Doped with RE Ions. Glass Phys. Chem. 44,
621 356–363.
622 Malfait, W.J., Zakaznova-Herzog, V.P., Halter, W.E., 2008. Quantitative Raman spectroscopy:
623 Speciation of Na-silicate glasses and melts. American Mineralogist 93, 1505–1518.
624 Malinovsky, V.K., Novikov, V.N., Sokolov, A.P., 1991. Log-normal spectrum of low-energy
625 vibrational excitations in glasses. Phys. Lett. A 153, 63–66.
626 Mastelaro, V.R., Zanotto, E.D., 2018. X-ray Absorption Fine Structure (XAFS) studies of oxide
627 glasses-A 45-year overview. Materials 11.
628 Mauro, J. C., Yue, Y.Z., Ellison, A.J., Gupta, P.K., Allan, D.C., 2009. Viscosity of glass-forming
629 liquids. Proc. Natl. Acad. Sci. USA 106, 19780–4.
630 McMillan, P., 1984. Structural studies of silicate glasses and melts-applications and limitations of
631 Raman spectroscopy. Am. Min. 69, 622–644.
632 McMillan, P.F., 1989. Raman spectroscopy in mineralogy and geochemistry. Annu. Rev. Earth
633 Planet. Sci. 17, 255–279.
634 Mercier, M., Di Muro, A., Giordano, D., Métrich, N., Lesne, P., Pichavant, M., Scaillet, B.,
635 Clocchiatti, R., Montagnac, G., 2009. Influence of glass polymerisation and oxidation on
636 micro-Raman water analysis in alumino-silicate glasses. Geochim. Cosmochim. Acta 73, 197–
637 217.
638 Moynihan, C.T., 1995. Structural relaxation and glass transition. Introduction: the nature of
639 structural relaxation, in: Structure, Dynamics, and Properties of Silicate Melts. pp. 1–20.
640 Mysen, B.O., 1990. Role of Al in depolymerized, peralkaline aluminosilicate melts in the systems
641 Li_2O-Al_2O_3-SiO_2, Na_2O-Al_2O_3-SiO_2, and K_2O-Al_2O_3-SiO_2. Am. Min. 75, 120–134.
642 Mysen, B.O., Finger, L.W., Virgo, D., Seifert, F.A., 1982. Curve-fitting of Raman spectra of
643 silicate glasses. Am. Min. 67, 686–695.
644 Mysen, B.O., Virgo, D., Seifert, F.A., 1982. The structure of silicate melts: Implications for
645 chemical and physical properties of natural magma. Rev. Geophys. 20, 353–383.

646 Neuville, D.R., Courtial, P., Dingwell, D.B., Richet, P., 1993. Thermodynamic and rheological
647 properties of rhyolite and andesite melts. Contrib. Mineral. Petrol. 113, 572–581.
648 Newhall, C.G., Punongbayan, R.S., 1996. The Narrow Margin of Successful Volcanic-Risk
649 Mitigation, in: Monitoring and Mitigation of Volcano Hazards. Springer Berlin Heidelberg, pp.
650 807–839.
651 Novikov, V.N., Sokolov, A.P., 2004. Poisson's ratio and the fragility of glass-forming liquids.
652 Nature 431, 961–963.
653 Okuno, M., Zotov, N., Schmücker, M., Schneider, H., 2005. Structure of SiO_2-Al_2O_3 glasses:
654 Combined X-ray diffraction, IR and Raman studies. J. Non Cryst. Solids. 351, 1032–1038.
655 Orsingher, L., Fontana, A., Gilioli, E., Carini, G., Carini, G., Tripodo, G., Unruh, T., Buchenau, U.,
656 2010. Vibrational dynamics of permanently densified GeO_2 glasses: Densification-induced
657 changes in the boson peak. J. Chem. Phys. 132, 124508.
658 Papale, P., 1999. Strain-induced magma fragmentation in explosive eruptions. Nature 397, 425–
659 428.
660 Phillips, W.A., 1979. Topology of covalent non-crystalline solids: Short-range order in
661 chalcogenide alloys. J. Non Cryst. Solids 34, 153–181.
662 Prata, G.S., Ventress, L.J., Carboni, E., Mather, T.A., Grainger, R.G., Pyle, D.M., 2019. A New
663 Parameterization of Volcanic Ash Complex Refractive Index Based on NBO/T and SiO_2
664 Content. J. Geophys. Res. 124, 1779–1797.
665 Richet, P., Lejeune, A.M., Holtz, F., Roux, J., 1996. Water and the viscosity of andesite melts.
666 Chem. Geol. 128, 185–197.
667 Romero, J.E., Morgavi, D., Arzilli, F., Daga, R., Caselli, A., Reckziegel, F., Viramonte, J., Díaz-
668 Alvarado, J., Polacci, M., Burton, M., Perugini, D., 2016. Eruption dynamics of the 22-23
669 April 2015 Calbuco Volcano (Southern Chile): Analyses of tephra fall deposits J. Volcanol.
670 Geotherm. 317, 15–29.
671 Scherer, G.W., 1984. Use of the Adam-Gibbs equation in the analysis of structural relaxation. J.
672 Am. Ceram. Soc. 67, 504–511.
673 Schirmacher, W., Ruocco, G., Scopigno, T., 2007. Acoustic attenuation in glasses and its relation
674 with the boson peak. Phys. Rev. Lett. 98, 1–4.
675 Scopigno, T., Ruocco, G., Sette, F., Monaco, G., 2003. Is the Fragility of a Liquid Embedded in the
676 Properties of Its Glass? Science 302, 849–852.
677 Sen, P.N., Thorpe, M.F., 1977. Phonons in AX_2 glasses: From molecular to band-like modes. Phys.
678 Rev. B 15, 4030–4038.
679 Shaw, H.R., 1972. Viscosities of magmatic silicate liquids; an empirical method of prediction. Am.
680 J. Sci. 272, 870–893.
681 Shebanova, O.N., Lazor, P., 2003. Raman spectroscopic study of magnetite ($FeFe_2O_4$): A new
682 assignment for the vibrational spectrum. J. Solid State Chem. 174, 424–430.
683 Shuker, R., Gammon, R.W., 1970. Raman-scattering selection-rule breaking and the density of
684 states in amorphous materials. Phys. Rev. Lett. 25, 222–225.
685 Stabile, P., Sicola, S., Giuli, G., Paris, E., Carroll, M.R.R., Deubener, J., Di Genova, D., 2021. The
686 effect of iron and alkali on the nanocrystal-free viscosity of volcanic melts: A combined
687 Raman spectroscopy and DSC study. Chem. Geol. 559, 119991.
688 Stillinger, F.H., 1988. Supercooled liquids, glass transitions, and the Kauzmann paradox. J. Chem.
689 Phys. 88, 7818–7825.
690 Taddeucci, J., Cimarelli, C., Alatorre-Ibargüengoitia, M.A., Delgado-Granados, H., Andronico, D.,
691 del Bello, E., Scarlato, P., di Stefano, F., 2021. Fracturing and healing of basaltic magmas
692 during explosive volcanic eruptions. Nat. Geosci. 14, 248–254.
693 Umari, P., Pasquarello, A., 2003. First-principles analysis of the Raman spectrum of vitreous silica:
694 comparison with the vibrational density of states, J. Phys. Condens. Matter 15, S1547.

Vetere, F., Holtz, F., 2021. Rheological Behavior of Partly Crystallized Silicate Melts Under Variable Shear Rate. Dynamic Magma Evolution, Geophysical Monograph, WILEY 1, 152–167.
Vetere, F., Iezzi, G., Perugini, D., Holtz, F., 2022. Rheological changes in melts and magmas induced by crystallization and strain rate. C. R. Geosci. 354.
Vetere, F., Murri, M., Alvaro, M., Domeneghetti, M.C., Rossi, S., Pisello, A., Perugini, D., Holtz, F., 2019. Viscosity of Pyroxenite Melt and Its Evolution During Cooling. J. Geophys. Res. Planets 124, 1451–1469.
Vetere, F., Petrelli, M., Perugini, D., Haselbach, S., Morgavi, D., Pisello, A., Iezzi, G., Holtz, F., 2021. Rheological evolution of eruptible Basaltic-Andesite Magmas under dynamic conditions: The importance of plagioclase growth rates. J. Volcanol. Geotherm. 420, 107411.
Vona, A., Romano, C., Dingwell, D.B., Giordano, D., 2011. The rheology of crystal-bearing basaltic magmas from Stromboli and Etna. Geochim. Cosmochim. Acta 75, 3214–3236.
Welsch, A.M., Knipping, J.L., Behrens, H., 2017. Fe-oxidation state in alkali-trisilicate glasses - A Raman spectroscopic study. J. Non Cryst. Solids 471, 28–38.
Whittington, A., Richet, P., Linard, Y., Holtz, F., 2001. The viscosity of hydrous phonolites and trachytes. Chem. Geol. 174, 209–223.
Zanatta, M., Baldi, G., Caponi, S., Fontana, A., Gilioli, E., Krish, M., Masciovecchio, C., Monaco, G., Orsingher, L., Rossi, F., Ruocco, G., Verbeni, R., 2010. Elastic properties of permanently densified silica: A Raman, Brillouin light, and x-ray scattering study. Phys. Rev. B 81, 4–7.
Zanatta, M., Fontana, A., Rossi, F., Gilioli, E., 2011. Effects of permanent densification on the vibrational density of states of vitreous silica. J. Non Cryst. Solids 357, 1892–1894.
Zhang, Y., 1999. A criterion for the fragmentation of bubbly magma based on brittle failure theory. Nature 402, 648–650.
Zheng, Q., Mauro, J.C., Ellison, A.J., Potuzak, M., Yue, Y., 2011. Universality of the high-temperature viscosity limit of silicate liquids. Phys. Rev. B. 83, 13–15.
Zheng, Q., Zhang, Y., Montazerian, M., Gulbiten, O., Mauro, J.C., Zanotto, E.D., Yue, Y., 2019. Understanding Glass through Differential Scanning Calorimetry. Chem Rev 119, 7848–7939.
Zheng, Q., Zheng, J., Solvang, M., Yue, Y., Mauro, J.C., 2020. Determining the liquidus viscosity of glass-forming liquids through differential scanning calorimetry. J. Am. Ceram. Soc.103, 6070–6074.
Zotov, N., Ebbsjö, I., Timpel, D., Keppler, H., 1999. Calculation of Raman spectra and vibrational properties of silicate glasses: Comparison between $Na_2Si_4O_9$ and SiO_2 glasses. Phys. Rev. B. 60, 6383–6397.

Figure 1

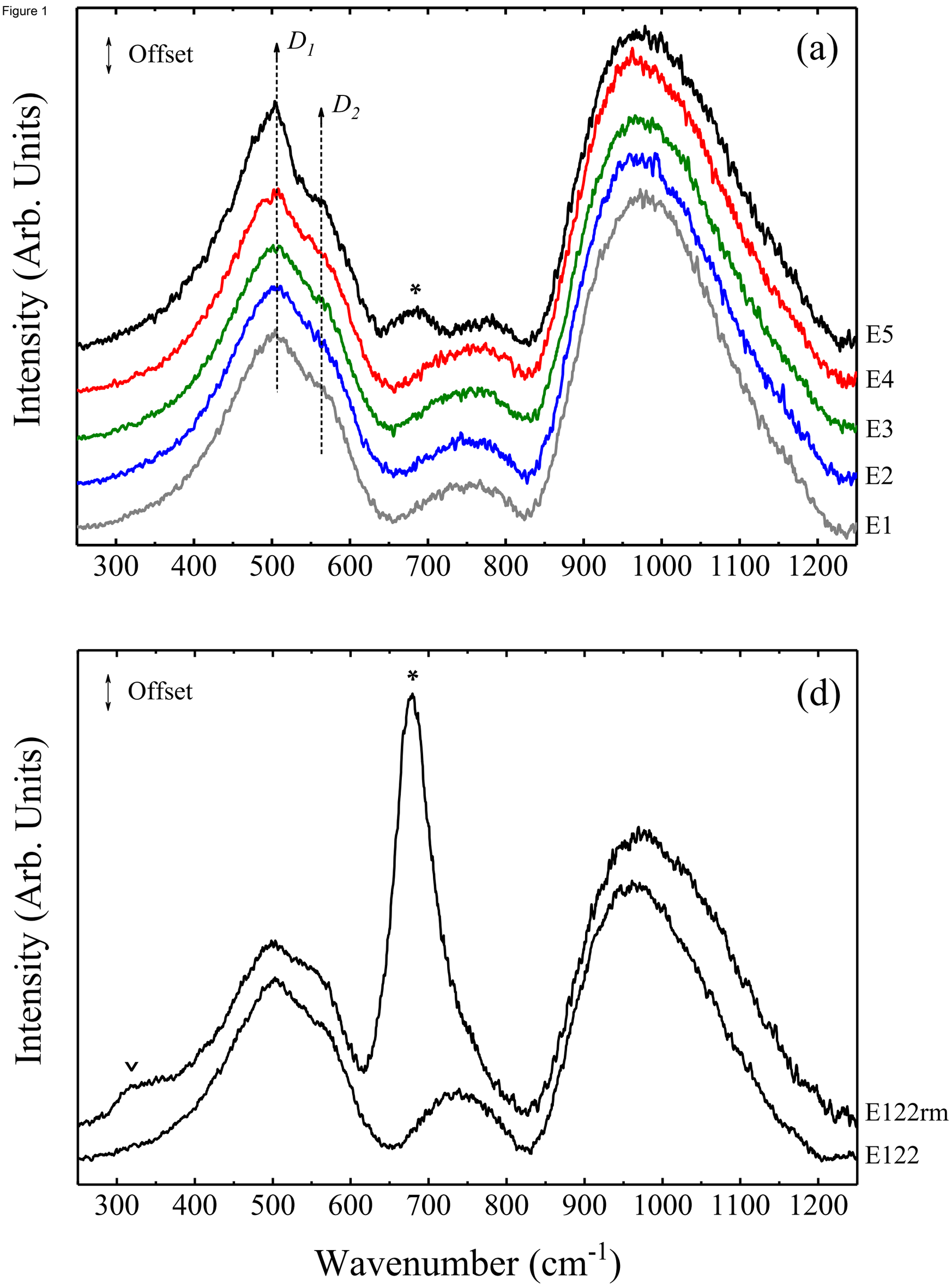

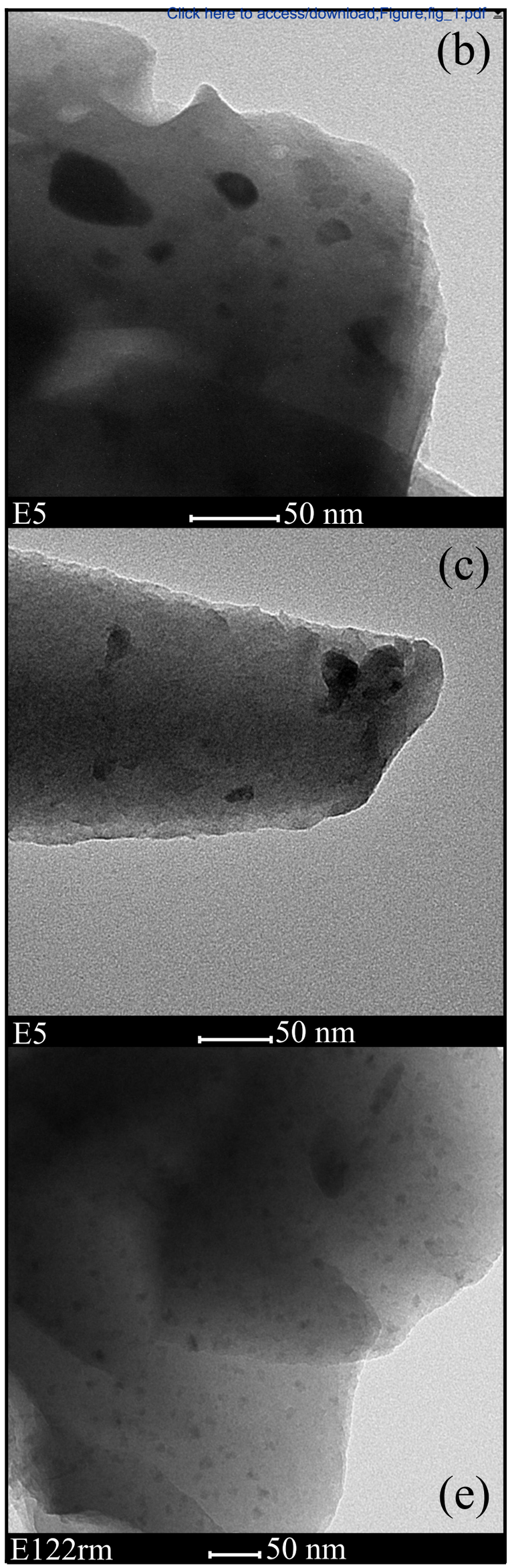

Figure 2

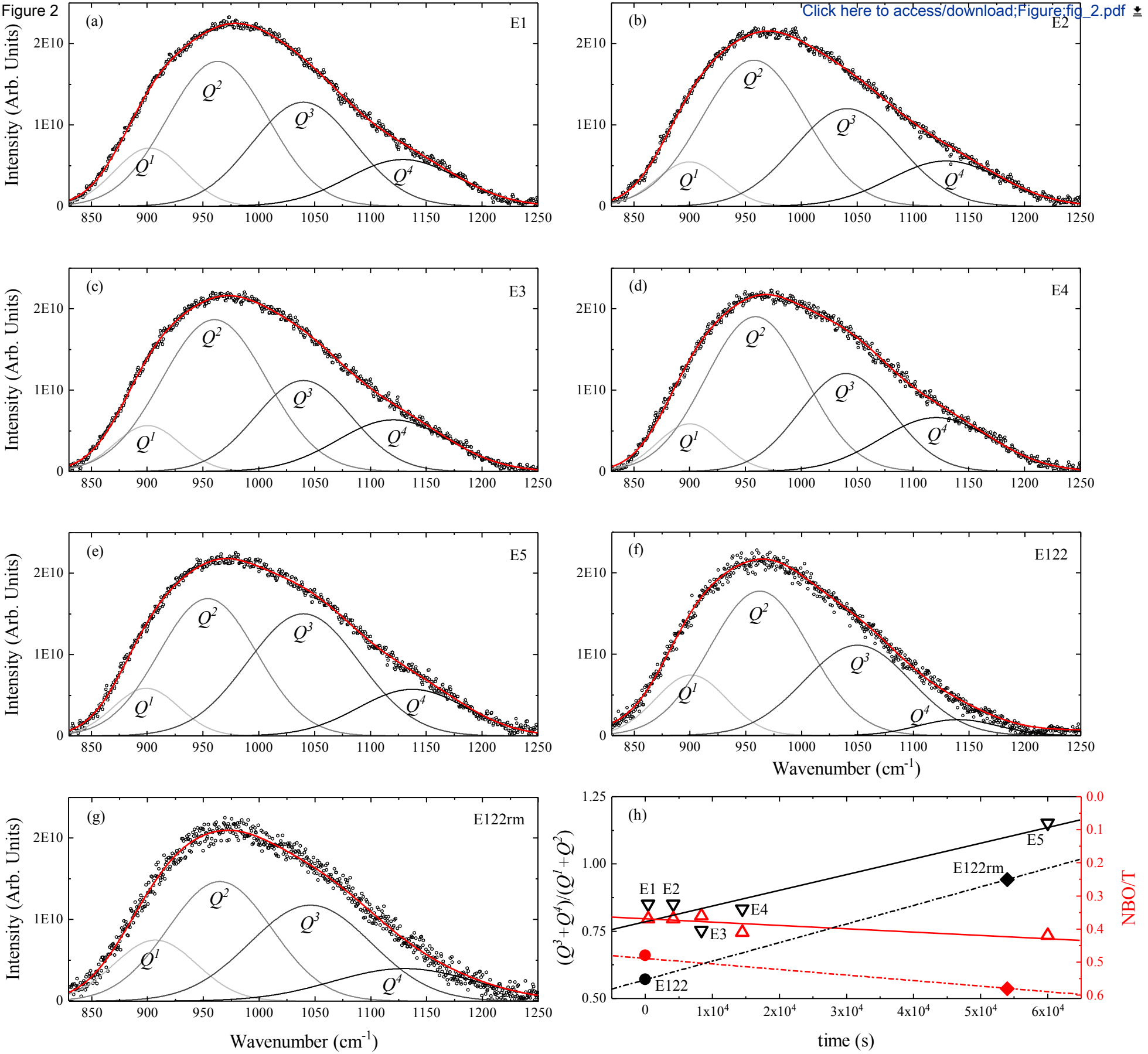

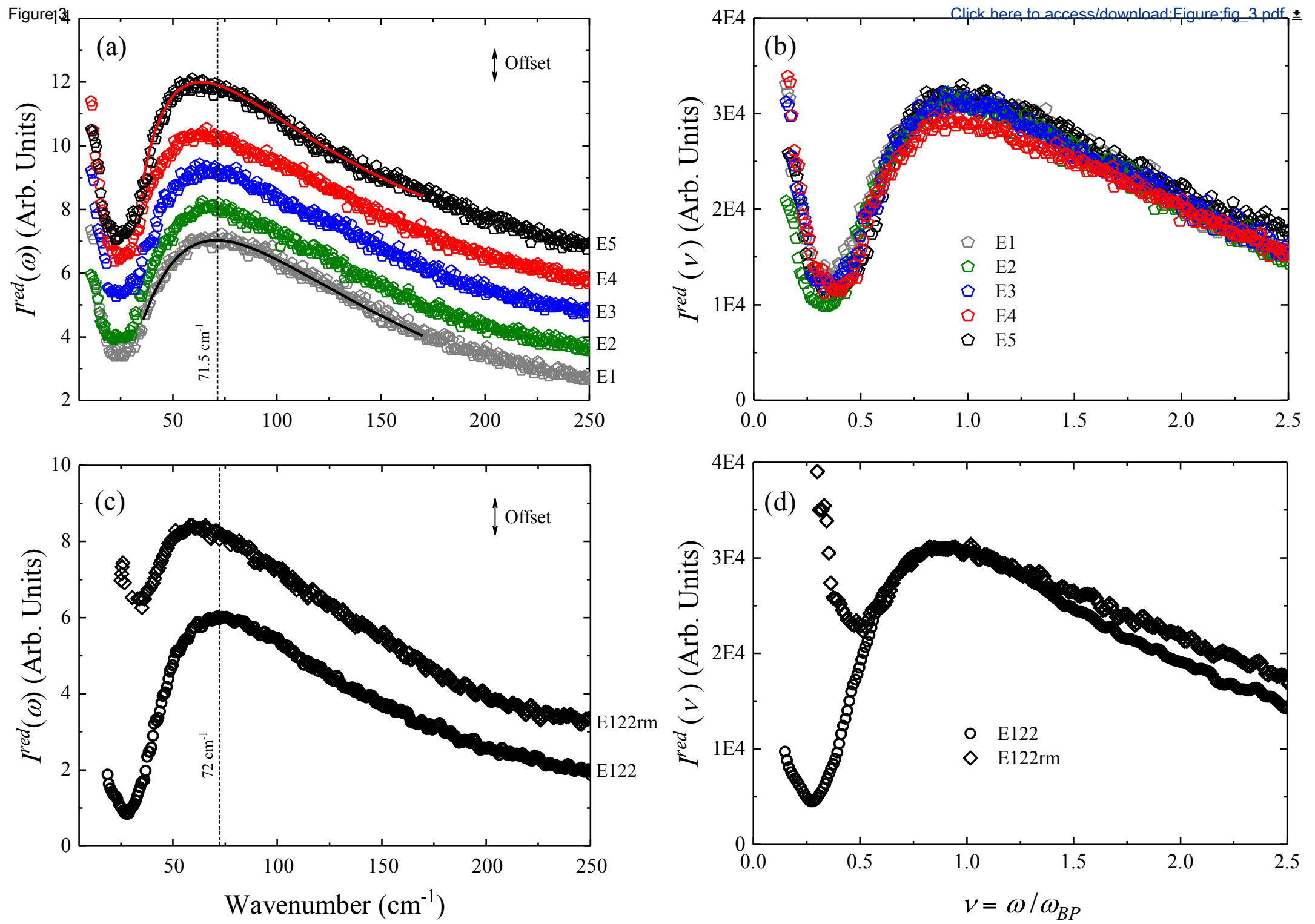

Figure 4

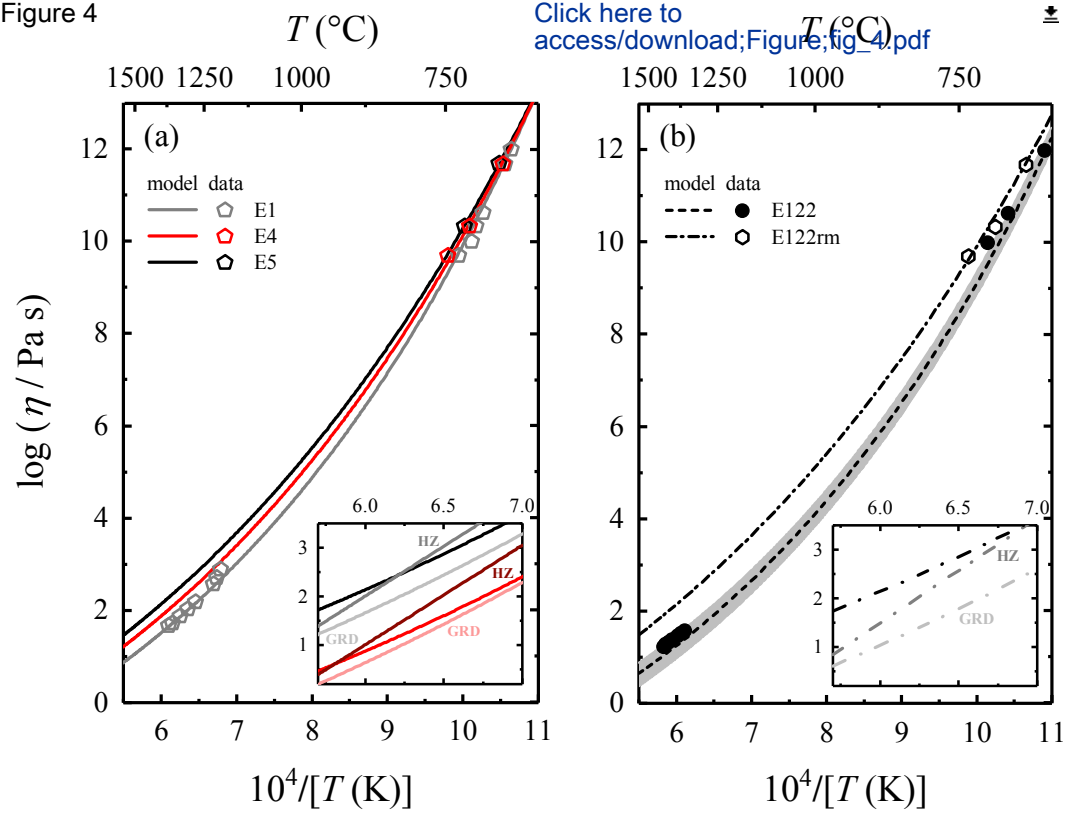

Declaration of interests

☒The authors declare that they have no known competing financial interests or personal relationships that could have appeared to influence the work reported in this paper.

☐The authors declare the following financial interests/personal relationships which may be considered as potential competing interests: